



## Abstract

As wind farms become larger, the spacing between turbines becomes a significant design element that imposes serious economic constraints. Effects of turbine spacing on the power produced and flow structure are crucial for future development of wind energy. To investigate the turbulent flow structures in a  $4 \times 3$  Cartesian wind turbine array, a wind tunnel experiment was carried out parameterizing the streamwise and spanwise wind turbine spacing. Four cases are chosen spacing turbines by 6 diameters ( $D$ ) or  $3D$  in the streamwise, and  $3D$  or  $1.5D$  in the spanwise direction. Data are obtained experimentally using stereo particle-image velocimetry. Mean streamwise velocity showed maximum values upstream of the turbine with the spacing of  $6D$  and  $3D$ , in the streamwise and spanwise direction, respectively. Fixing the spanwise turbine spacing to  $3D$ , variations in the streamwise spacing influence the turbulent flow structure and the power available to following wind turbines. Quantitative comparisons are made through spatial averaging, shifting measurement data and interpolating to account for the full range between devices to obtain data independent of array spacing. The largest averaged Reynolds stress is seen in cases with spacing of  $3D \times 3D$ . Snapshot proper orthogonal decomposition (POD) was employed to identify the flow structures based on the turbulence kinetic energy content. The maximum turbulence kinetic energy content in the first POD mode compared with other cases is seen for turbine spacing of  $6D \times 1.5D$ . The flow upstream of each wind turbine converges faster than the flow downstream according to accumulation of turbulence kinetic energy by POD modes, regardless of spacing. The streamwise-averaged profile of the Reynolds stress is reconstructed using a specific number of modes for each case; the case of  $6D \times 1.5D$  spacing shows the fastest reconstruction. Intermediate modes are also used to reconstruct the averaged profile and show that the intermediate scales are responsible for features seen in the original profile. The variation in streamwise and spanwise spacing leads to changes in the background structure of the turbulence, where the color map based on barycentric map and anisotropy stress tensor provides a new perspective on the nature of the perturbations within the wind turbine array. The impact of the streamwise and spanwise spacings on power produced is quantified, where the maximum production corresponds with the case of greatest turbine spacing.

## 6 I. INTRODUCTION

7 Allowing insufficient space between wind turbines in an array leads to decreased perfor-  
8 mance through wake interaction, decreased wind velocity and an increase in the accumulated  
9 fatigue loads and intermittency events on downstream turbines (Viggiano et al. 2016, Ali  
10 et al. 2016a). Wind turbine wakes lead to an average loss of 10-20% of the total potential  
11 power output of wind turbine array (Barthelmie et al. 2007). Extensive experimental and  
12 numerical studies focus on wake properties in terms of the mean flow characteristics used to  
13 obtain estimates of power production (Chamorro and Porté-Agel 2009, 2011). Wake growth  
14 depends on the shape and magnitude of the velocity deficit, surface roughness, flow above  
15 the canopy and spacing between the turbines.

16 Although there are many studies dealing with the effect of the density of turbines on  
17 the wake recovery, it is still a debated question. The actual spacing of wind turbines can  
18 vary greatly from one array to another. For example, in the Nysted farm, spacing is 10.5  
19 diameters ( $D$ ) downstream by  $5.8D$  spanwise at the exact row (ER). The wind direction at  
20 the ER is  $278^\circ$  and mean wind direction can slightly offset from ER by  $\pm 15^\circ$  (Barthelmie  
21 et al. 2010). Of relevance, the variability in the wind direction pertains to the center of the  
22 wake, assesses the wake width, and the character of wake behavior. In the Horns Rev farm,  
23 spacing between devices is  $7D$ , although aligned with the bulk flow direction spacing is as  
24 much as  $10.4D$ . Barthelmie and Jensen (2010) showed that the spacing in the Nysted farm  
25 is responsible for 68-76% of the farm efficiency variation. Hansen et al. (2012) pointed out  
26 that variations in the power deficit are almost negligible when spacing is approximately  $10D$   
27 at the Horns Rev farm, in contrast to limited spacings that present a considerable power  
28 deficit. González-Longatt et al. (2012) found that when the streamwise and spanwise spacing  
29 increased, the wake coefficient, which represents the ratio of total power output with and  
30 without wake effects, is increased. Further, the effect of the incoming flow direction on the  
31 wake coefficient increased when the spacing of the array is reduced. Meyers and Meneveau  
32 (2012) studied the optimal spacing in a fully developed wind farm under neutral stratification  
33 and flat terrain. The results highlighted that, depending on the ratio of land and turbine  
34 costs, the optimal spacing might be  $15D$  instead of  $7D$ . Stevens (2015) pronounced that the  
35 optimal spacing depends on the length of the wind farm in addition to the factors suggested  
36 in Meyers and Meneveau (2012). Orography and wind direction are relevant when deciding

37 distance between turbines as well as layout as shown by Romanic et al. (2018). Nilsson  
38 et al. (2015) performed large eddy simulations (LES) of the Lillgrund wind farm, where pre-  
39 generated turbulence and wind shear are imposed in the computational domain to simulate  
40 realistic atmospheric conditions. In the Lillgrund wind farm, the actual spacing is  $3.3D$  and  
41  $4.6D$  in the streamwise and spanwise directions. A turbine is missing near to the center of the  
42 wind farm, demonstrating the effects of a farm with limited spacing and one with sufficient  
43 spacing in otherwise identical operating conditions. The results of Nilsson et al. (2015) are  
44 highly applicable in the current study, although their foci are on turbulence intensity effects  
45 and yaw angle.

46 Further investigations in array optimization have been undertaken by changing the align-  
47 ment of the wind farm, often referred to as staggered wind farms. Meyers and Meneveau  
48 (2010) compared aligned versus staggered wind farms; the latter yielding a 5% increase in  
49 extracted power. Yang et al. (2012) used LES to study the influence of the streamwise and  
50 spanwise spacing on the power output in aligned wind farms under fully developed regime.  
51 Their work confirmed that power produced by the turbines scales with streamwise spacing  
52 more than with the spanwise spacing. Wu and Porté-Agel (2013) investigated turbulent flow  
53 within and above aligned and staggered wind farms under neutral condition. Cumulative  
54 wakes are shown to be subject to strong lateral interaction in the staggered case. In contrast,  
55 lateral interaction is negligible in the aligned wind farm. Archer et al. (2013) quantified the  
56 influence of wind farm layout on the power production, verifying that increasing the turbine  
57 spacing in the predominant wind direction maximized the power production, regardless of  
58 device arrangement in the wind farm. Stevens et al. (2016) investigated the power output  
59 and wake effects in aligned and staggered wind farms with different streamwise and spanwise  
60 turbine spacings. In the staggered configuration, power output in a fully developed flow de-  
61 pends mainly on the spanwise and streamwise spacings, whereas in the aligned configuration,  
62 power strongly depends on the streamwise spacing.

63 As wind farms become larger, the land costs and availability represent critical factors in  
64 the overall value of the wind farm. Spacing between the turbines is an important design  
65 factor in terms of overall wind farm performance and economic constraints. Investigation of  
66 wind farms with limited spacing is important in order to quantify the effects of wind turbine  
67 wake interaction on the power production. The current work compares the turbulent flow  
68 in various configurations of the array, where the streamwise and spanwise spacings are var-

69 ied. The tunnel-scaled wind farm is, however, restricted to a flat surface and topographic  
70 influences are not considered, although the inflow to the wind farm includes modifications  
71 to more closely resemble an atmospheric boundary layer. The performance of the arrays  
72 is characterized by analyzing the mean velocity, Reynolds shear stress, and power produc-  
73 tion. Proper orthogonal decomposition (POD) is employed to identify coherent structures of  
74 the turbulent wake associated with variations in spacing. The Reynolds stresses are recon-  
75 structed from POD basis, demonstrating variation in rates of convergence according to wind  
76 turbine spacing. Finally the anisotropy stress tensor is discussed to quantify the structure  
77 of the stress tensor based on the invariant for the various spacings.

## 78 II. THEORY

### 79 A. Snapshot Proper Orthogonal Decomposition

80 POD is a mathematical tool that derives optimal basis functions from a set of measure-  
81 ments, decomposing the flow into modes that express the most dominant features. The  
82 technique, which was presented in the frame of turbulence by Lumley (1967), categorizes  
83 structures within the turbulent flow depending on their energy content. Sirovich (1987)  
84 presented the snapshot POD, that relaxes the computational difficulties of the classical or-  
85 thogonal decomposition. POD has been used to describe coherent structures for different  
86 flows, such as axisymmetric mixing layer (Glauser and George 1987), channel flow (Moin  
87 and Moser 1989), atmospheric boundary layer (Shah and Bou-Zeid 2014), wake behind disk  
88 (Tutkun et al. 2008), and wind turbine wake flow (Andersen et al. 2013, Bastine et al. 2014,  
89 VerHulst and Meneveau 2014, Hamilton et al. 2015a, Ali et al. 2016b, 2017a).

90 The flow field, taken as the fluctuating velocity after subtracting time average mean  
91 velocity from instantaneous velocity, can be represented as  $u = u(\vec{x}, t^n)$ , where  $\vec{x}$  and  $t^n$   
92 refer to the spatial coordinates and time at sample  $n$ , respectively. A set of the orthonormal  
93 basis functions,  $\phi$ , can be presented as

$$\phi = \sum_{n=1}^N A(t^n)u(\vec{x}, t^n), \quad (1)$$

94 where  $N$  is the number of snapshots. The largest projection can be determined using the  
95 two point correlation tensor and Fredholm integral equation

$$\int_{\Omega} \frac{1}{N} \sum_{n=1}^N u(\vec{x}, t^n) u^T(\vec{x}', t^n) \phi(\vec{x}') d\vec{x}' = \lambda \phi(\vec{x}), \quad (2)$$

96 where left hand side of the equation presents a spatial correlation between two points  $\vec{x}$   
 97 and  $\vec{x}'$ ,  $T$  signifies the transpose of a matrix,  $\Omega$  is the physical domain, and  $\lambda$  are the  
 98 eigenvalues. To acquire the optimal basis functions, the problem is reduced to an eigenvalue  
 99 decomposition denoted as  $[C][G] = \lambda[G]$ , where  $C$ ,  $G$  and  $\lambda$  are the correlation tensor, basis  
 100 of eigenvectors, and eigenvalues, respectively. The matrix  $[G]$  is related to the time coefficient  
 101 as  $[G] = [A(t^1), A(t^2), \dots, A(t^N)]^T$ . The POD eigenvectors illustrate the spatial structure  
 102 of the turbulent flow and the eigenvalues measure the energy associated with corresponding  
 103 eigenvectors. The summation of the eigenvalues presents the total turbulent kinetic energy  
 104 ( $E$ ) in the flow domain. The cumulative kinetic energy fraction  $\eta$  and the normalized energy  
 105 content of each mode  $\xi$  can be represented as  $\eta_n = \sum_{j=1}^n \lambda_n / \sum_{j=1}^N \lambda_n$  and  $\xi_n = \lambda_n / \sum_{j=1}^N \lambda_n$ .  
 106 POD is particularly useful in rebuilding the Reynolds shear stress using a limited set ( $N_{lm}$ )  
 107 of eigenfunctions as follows,

$$\langle u_i u_j \rangle = \sum_{n=1}^{N_{lm}} \lambda_n \phi_i^n \phi_j^n. \quad (3)$$

## 108 B. Anisotropy Stress Tensor

109 Turbulence is often described through the Reynolds stress tensor. Rotta (1951) developed  
 110 the Reynolds stress anisotropy tensor, as  $a_{ij} = \overline{u_i u_j} - \frac{2}{3} k \delta_{ij}$ , where  $\delta_{ij}$  is the Kronecker delta  
 111 and  $k$  represents the turbulence kinetic energy and is defined by  $k = 0.5 \sum_{i=1}^3 \langle u_i u_i \rangle$ . The  
 112 deviatoric tensor is obtained,  $b_{ij} = \overline{u_i u_j} / \overline{u_k u_k} - \frac{1}{3} \delta_{ij}$ . The second and third scalar invariants  
 113 are defined as  $6\eta^2 = b_{ij} b_{ji}$  and  $6\xi^3 = b_{ij} b_{jk} b_{ki}$ , respectively (see Pope (2000), Lumley and  
 114 Newman (1977) for more details). The second invariant,  $\eta$ , measures the degree of the  
 115 anisotropy and the third invariant,  $\xi$ , specifies the state of turbulence. Alternatively, the  
 116 eigenvalue decomposition of the normalized Reynolds stress anisotropy tensor can be used to  
 117 derive the the second and third invariants as  $\eta^2 = \frac{1}{3} (\lambda_1^2 + \lambda_1 \lambda_2 + \lambda_2^2)$  and  $\xi^3 = -\frac{1}{2} \lambda_1 \lambda_2 (\lambda_1 + \lambda_2)$ .  
 118 In an attempt to further facilitate the study of turbulence anisotropy, Banerjee et al. (2007)  
 119 presented a linearized anisotropy tensor invariants, termed barycentric map (BM) as follows,

TABLE I: Summary of the special turbulence cases described by the barycentric map.

Cases	Eigenvalues
Three-component	$\lambda_1 = \lambda_2 = \lambda_3 = 0$
Two-component	$\lambda_1 = \lambda_2 = \frac{1}{6}, \lambda_3 = -\frac{1}{3}$
One-component	$\lambda_1 = \frac{2}{3}, \lambda_2 = \lambda_3 = -\frac{1}{3}$

$$\hat{b}_{ij} = C_{1c} \begin{pmatrix} 2/3 & 0 & 0 \\ 0 & -1/3 & 0 \\ 0 & 0 & -1/3 \end{pmatrix} + C_{2c} \begin{pmatrix} 1/6 & 0 & 0 \\ 0 & 1/6 & 0 \\ 0 & 0 & -1/3 \end{pmatrix} + C_{3c} \begin{pmatrix} 0 & 0 & 0 \\ 0 & 0 & 0 \\ 0 & 0 & 0 \end{pmatrix}, \quad (4)$$

120 where  $C_{1c}$ ,  $C_{2c}$  and  $C_{3c}$  are the coefficients that represent the boundary of the barycentric  
121 map. The BM coefficients are determined as  $C_{1c} = \lambda_1 - \lambda_2$ ,  $C_{2c} = 2(\lambda_2 - \lambda_3)$ , and  $C_{3c} =$   
122  $3\lambda_3 + 1$ . The three basis matrices in equation (4) represent the three vertices of the equilateral  
123 triangle, with the following coordinates  $(x_{1c}, y_{1c})$ ,  $(x_{2c}, y_{2c})$  and  $(x_{3c}, y_{3c})$ . Table I presents  
124 the three turbulence states corresponding with the vertices of the BM, which also correspond  
125 to either isotropic (three-component), one- or two-component turbulence. As a result, any  
126 realizable turbulence state can be represented as follows,

$$x_{new} = C_{1c}x_{1c} + C_{2c}x_{2c} + C_{3c}x_{3c}, \quad (5)$$

$$y_{new} = C_{1c}y_{1c} + C_{2c}y_{2c} + C_{3c}y_{3c}. \quad (6)$$

127 Emory and Iaccarino (2014) also introduced a color map based visualization technique that  
128 aids to interpret the spatial distribution of the normalized anisotropy tensor. In this case,  
129 they attributed to each vertex of the barycentric map an RGB (Red-Green-Blue) color, see  
130 figure 1 for more details. This color map technique combines the coefficients  $C_{1c}$ ,  $C_{2c}$  and  
131  $C_{3c}$  to generate an RGB map such that,

$$\begin{bmatrix} R \\ G \\ B \end{bmatrix} = C_{1c}^* \begin{bmatrix} 1 \\ 0 \\ 0 \end{bmatrix} + C_{2c}^* \begin{bmatrix} 0 \\ 1 \\ 0 \end{bmatrix} + C_{3c}^* \begin{bmatrix} 0 \\ 0 \\ 1 \end{bmatrix}. \quad (7)$$

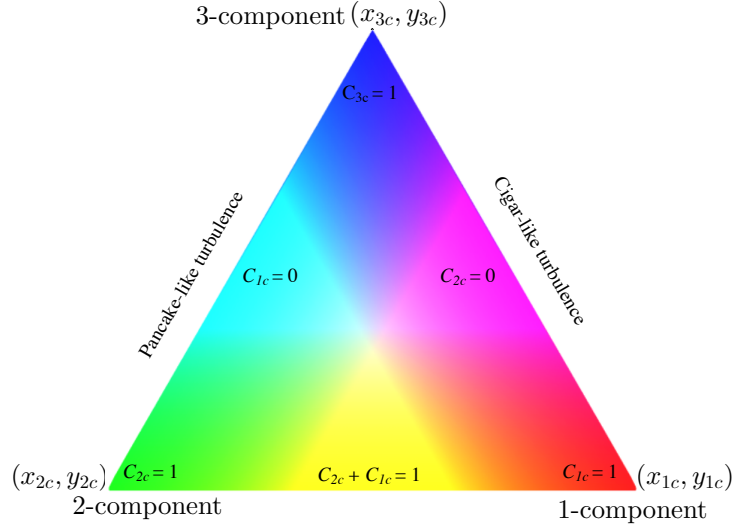


FIG. 1: Schematic representation of the Barycentric map (BM) with color map.

132 where  $C_{ic}^*$  are the modified coefficients that can be determined as  $C_{ic}^* = (C_{ic} + 0.65)^5$ . The  
 133 coefficient with value of (0.65 and 5) is applied as it provides the optimal visualization; other  
 134 coefficients are tested with less success in terms of marking differences. As a result, one-  
 135 component turbulence is associated to the red color, two-component turbulence to green,  
 136 and three-component (isotropic turbulence) to blue, see figure 1. The anisotropy has been  
 137 examined in different types of flow, including pipe and duct flows (Antonia et al. 1991,  
 138 Krogstad and Torbergsen 2000), atmospheric boundary layer (Klipp 2010, 2012) as well as  
 139 the wake of a wind turbine (Gómez-Elvira et al. 2005, Hamilton and Cal 2015, Ali et al.  
 140 2017b,c). Here we will used the anisotropy stress tensor is employed to quantify the effect  
 141 of the spacing on the turbulence states.

### 142 III. EXPERIMENTAL DESIGN

143 A  $4 \times 3$  array of wind turbines is placed in the closed-circuit wind tunnel at Portland  
 144 State University to study the effects due to variation in streamwise and spanwise spacing in  
 145 a wind turbine array. The dimensions of the wind tunnel test section are 5 m (long), 1.2 m  
 146 (wide) and 0.8 m (high). The blockage ratio is less than 5% in the test section. The entrance  
 147 of the test section is conditioned by the passive grid, which consists of 7 horizontal and 6  
 148 vertical rods, to introduce large-scale turbulence. Nine vertical acrylic strakes, located at

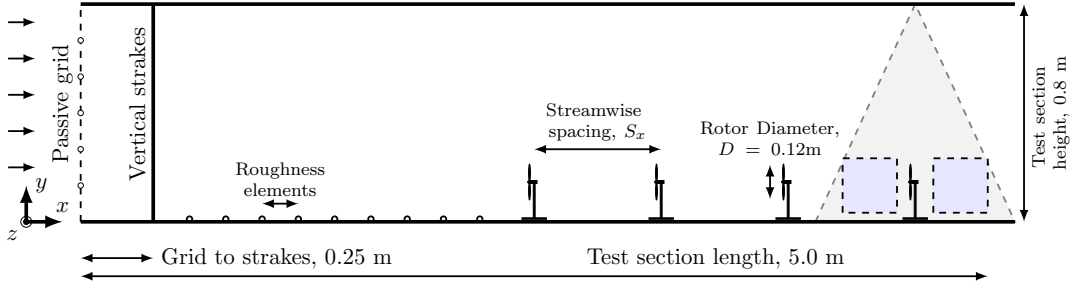


FIG. 2: Experimental Setup. Dashed gray lines indicate the placement of the laser sheet relative to the model wind turbine array. Filled gray boxes indicate measurement locations discussed below.

149 0.25 m downstream of the passive grid and 2.15 m upstream of the first row of the wind  
 150 turbine, are used to modify the inflow. The thickness of the strakes is 0.0125 m and are  
 151 spaced every 0.136 m across the test section. Surface roughness was introduced to the wall  
 152 as a series of chains with a diameter of 0.0075 m, spaced 0.11 m apart. Figure 2 shows the  
 153 schematic of the experimental setup.

154 Sheet steel of 0.0005 m thick is used to construct the 3-bladed wind turbine rotors.  
 155 The diameter of the rotor is  $D = 0.12$  m, equal to the height of the turbine tower. The  
 156 scaled turbine models are manufactured in-house. Based on full scale turbines with a 100  
 157 m rotor diameter and a 100 m hub height, the scaled models are at 1:830 scale. In this  
 158 study, the Reynolds number in the entrance row turbines is approximately the same order  
 159 of magnitude of the independent range detailed in Chamorro et al. (2012). The rotor blades  
 160 are steel sheets laser cut to shape and are 0.0005 m thick. The blades are shaped using a die  
 161 press. The die press is designed in-house to produce a 15 degree pitch from the plane of the  
 162 rotor and a 10 degree twist at the tip. Figure 3 presents the schematic of the wind turbine  
 163 model. The wind turbine model design used is that presented in Cal et al. (2010), Kang and  
 164 Meneveau (2010) and Hamilton et al. (2015b). Operating conditions for the wind turbines  
 165 are also scaled, namely the power coefficient,  $C_p$  and tip-speed ratio,  $\lambda$ , which are detailed  
 166 in Hamilton et al. (2015b) The streamwise integral length scale is approximately 0.13 m,  
 167 which is the same order of magnitude as the turbine rotor and representative of conditions  
 168 seen by full-scale turbines in atmospheric flows. A DC electrical motor of 0.0013 m diameter  
 169 and 0.0312 m long formed the nacelle of the turbine and is aligned with the flow direction.  
 170 A torque-sensing system is connected to the DC motor shaft following the design outlined  
 171 in Kang and Meneveau (2010). The torque sensor consists of a strain gauge, Wheatstone

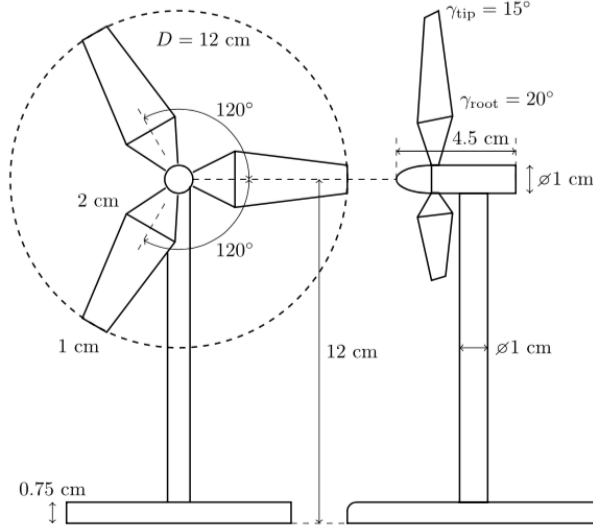


FIG. 3: Schematic representation of the wind turbine model (Hamilton and Cal 2015).

172 bridge and the Data Acquisition with measuring software to collect the data.

173 The flow field is sampled in four configurations of a model-scale wind turbine array,  
 174 classified as  $C_{S_x \times S_z}$ , shown in Table II. Permutations of the streamwise spacing ( $S_x$ ) of  $6D$   
 175 and  $3D$  and spanwise spacing ( $S_z$ ) of  $3D$  and  $1.5D$  are examined. Stereoscopic particle image  
 176 velocimetry (SPIV) is used to measure streamwise, wall-normal and spanwise instantaneous  
 177 velocity at the upstream and downstream of the wind turbine at the center line of the  
 178 fourth row as shown in figure 4. At each measurement location, 2000 images are taken,  
 179 to ensure convergence of second-order statistics. The sampling rate of the SPIV system is  
 180 fixed at 5 Hz. SPIV equipment is LaVision and consists of a Nd:Yag (532nm, 1200mJ, 4ns  
 181 duration) double-pulsed laser and four 4 MP ImagerProX CCD cameras positioned for the  
 182 upstream and downstream of the wind turbine. Neutrally buoyant fluid particles of diethyl  
 183 hexyl sebacate are introduced to the flow and allowed to mix. Consistent seeding density is  
 184 maintained in order to mitigate measurement errors. The laser sheet is approximately 0.001  
 185 m thick with less than 5 mrad divergence angle. Each measurement window is  $0.2 \text{ m} \times 0.2$   
 186 m aligned with the center of each turbine, parallel to the bulk flow. A multi-pass fast Fourier  
 187 transformation is used to process the raw data into vector fields. Erroneous measurement  
 188 of the vector fields are replaced using Gaussian interpolation of neighboring vectors. Based  
 189 on the variability estimator (George 2013), the error of the SPIV measurements is on the  
 190 order of 3%. The major uncertainty pertaining to the out-of-plane (spanwise) component.

TABLE II: Streamwise and spanwise spacing of the experimental tests.

Cases	$S_x$	$S_z$	Occupied Area
$C_{6 \times 3}$	$6D$	$3D$	$18D^2$
$C_{3 \times 3}$	$3D$	$3D$	$9D^2$
$C_{3 \times 1.5}$	$3D$	$1.5D$	$4.5D^2$
$C_{6 \times 1.5}$	$6D$	$1.5D$	$9D^2$

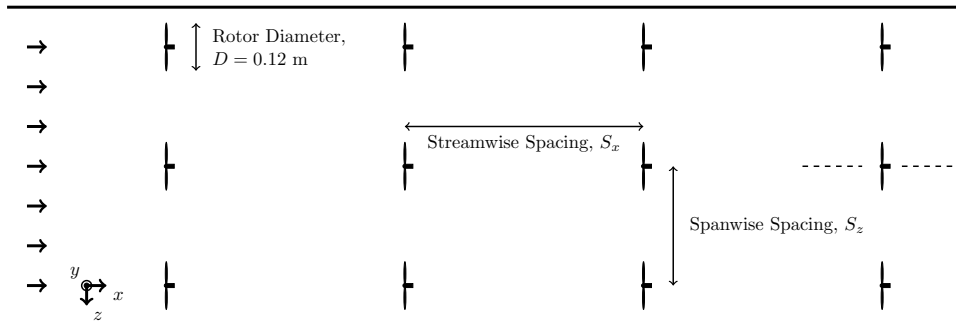


FIG. 4: Top view of 4 by 3 wind turbine array. The dash lines at the last row centerline turbine represent the measurement locations.

## 191 IV. RESULTS

### 192 A. Statistical Analysis.

193 Characterization of the wind turbine wake flow is presented by the streamwise mean  
 194 velocity and Reynolds shear stress, with the aim to understand the influence of turbine-  
 195 to-turbine spacing. Figure 5 presents the streamwise normalized mean velocity,  $U/U_\infty$ ,  
 196 upstream and downstream of each wind turbine for the cases  $C_{6 \times 3}$ ,  $C_{3 \times 3}$ ,  $C_{3 \times 1.5}$  and  $C_{6 \times 1.5}$ .  
 197 The inflow mean velocity at the hub height  $U_\infty$  is used in the normalization, where  $U_\infty =$   
 198  $5.5 \text{ m s}^{-1}$ . The left and right contour plots of each case present the flow upstream and  
 199 downstream of each turbine, respectively. At upstream measurement window, case  $C_{6 \times 3}$   
 200 exhibits the largest streamwise mean velocities due to greater recovery of the flow upstream  
 201 of the turbine. Although the streamwise spacing of case  $C_{6 \times 1.5}$  is similar that of case  $C_{6 \times 3}$ ,  
 202 the former shows reduced hub height velocity. The normalized mean velocity is about 0.567  
 203 compared with 0.66 in case  $C_{6 \times 3}$ , confirming the influence of the spanwise spacing on wake  
 204 evolution and flow recovery. Variations perceived between case  $C_{3 \times 3}$  and  $C_{3 \times 1.5}$  are small,

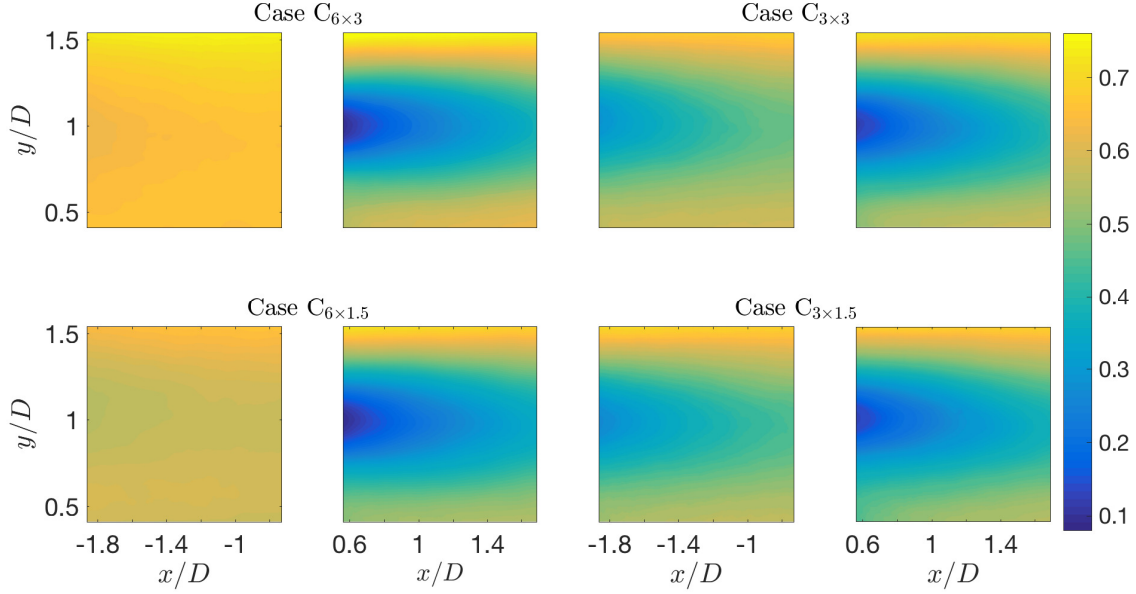


FIG. 5: Normalized streamwise velocity,  $U/U_\infty$ , at upstream and downstream of the cases  $C_{6\times 3}$ ,  $C_{3\times 3}$ ,  $C_{3\times 1.5}$ , and  $C_{6\times 1.5}$ .

205 where case  $C_{3\times 3}$  demonstrates higher velocities by approximately 2%. Downstream of the  
 206 turbine, the four cases show more relevant differences especially above the top tip and below  
 207 the bottom tip, where case  $C_{6\times 3}$ , once again, shows the greatest velocities by approximately  
 208 20%. Case  $C_{3\times 3}$  also shows higher velocities below the bottom tip compared with cases  
 209  $C_{3\times 1.5}$  and  $C_{6\times 1.5}$ . The normalized mean streamwise velocity and the turbulence intensity in  
 210 Nilsson et al. (2015) showed similar compound wakes from the upstream and downstream  
 211 turbines and confirmed the current result of cases  $C_{3\times 3}$  and  $C_{3\times 1.5}$ . In that study, there was  
 212 one location with an absent turbine and the flow was given extra space for recovery. The  
 213 recovered wake flow in Nilsson et al. (2015) is similar to the present cases  $C_{6\times 3}$  and  $C_{6\times 1.5}$ .

214 Figure 6 compares the in-plane normalized Reynolds shear stress  $-\overline{uv}/U_\infty^2$  for all test  
 215 cases. The fluctuating velocities in streamwise and wall-normal direction are denoted as  $u$   
 216 and  $v$ , respectively. In the upstream window, cases  $C_{3\times 3}$  and  $C_{3\times 1.5}$  display higher stress  
 217 compared with  $C_{6\times 3}$  and  $C_{6\times 1.5}$ . Although the spanwise spacing of case  $C_{3\times 1.5}$  is half of  
 218 case  $C_{3\times 3}$ , no relevant differences are apparent. In the downstream window, comparison  
 219 indicates that reducing streamwise spacing increases the Reynolds shear stress. The average  
 220 value of the shear stress in the wake is 16% greater for  $C_{3\times 3}$  than for  $C_{6\times 3}$ . A similar effect is  
 221 observed in case  $C_{3\times 1.5}$ , where average value of the stress is 2% greater than that of  $C_{6\times 1.5}$ .

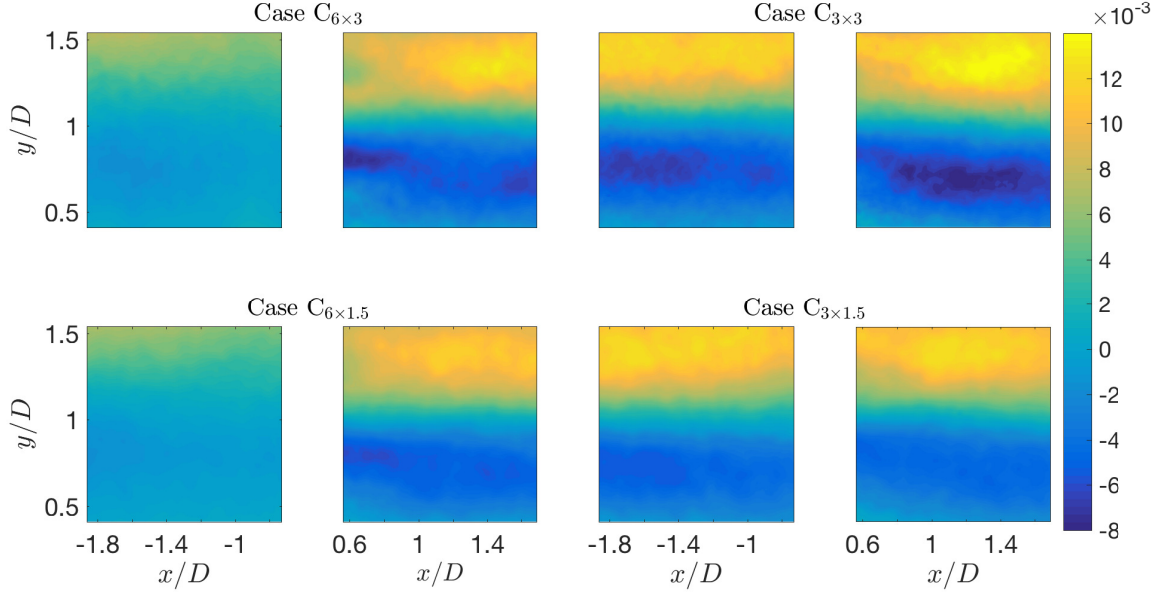


FIG. 6: Normalized Reynolds shear stress,  $-\overline{uv}/U_\infty^2$ , in upstream and downstream of the each measurement case.

222 The effect of spanwise spacing is more pronounced when the streamwise spacing is  $3D$ ; the  
 223 average shear stress is approximately 20% greater in  $C_{3 \times 1.5}$  than in  $C_{3 \times 3}$ .

## 224 B. Averaged Profiles.

225 Spatial averaging of the flow statistics is undertaken by moving the upstream domain  
 226 of each case beyond its corresponding downstream domain and performing streamwise av-  
 227 eraging, following the procedure in Cal et al. (2010). Though the spatial averaging, it is  
 228 possible to compare key data from different cases taking into account the different streamwise  
 229 spacings. Streamwise averaging is denoted by  $\langle \cdot \rangle_x$ . Figure 7(a) shows profiles of streamwise-  
 230 averaged mean velocity for all four cases. Cases  $C_{6 \times 3}$  and  $C_{3 \times 1.5}$  show the largest and  
 231 smallest velocity deficits, respectively. At hub height, the velocity of the case  $C_{6 \times 3}$  is ap-  
 232 proximately  $2.25 \text{ m s}^{-1}$  whereas case  $C_{3 \times 1.5}$  shows a velocity of approximately  $1.6 \text{ m s}^{-1}$ .  
 233 Comparing to  $C_{6 \times 3}$ , the change seen in the spatially-averaged velocity is greater in  $C_{3 \times 3}$   
 234 than in  $C_{6 \times 1.5}$ , confirming that the impact of reducing streamwise spacing is greater than  
 235 changing the spanwise spacing. Interestingly, a reduction in streamwise spacing shows less  
 236 effect when the spanwise spacing  $S_z = 1.5D$ . This is a result due to constraining the wake

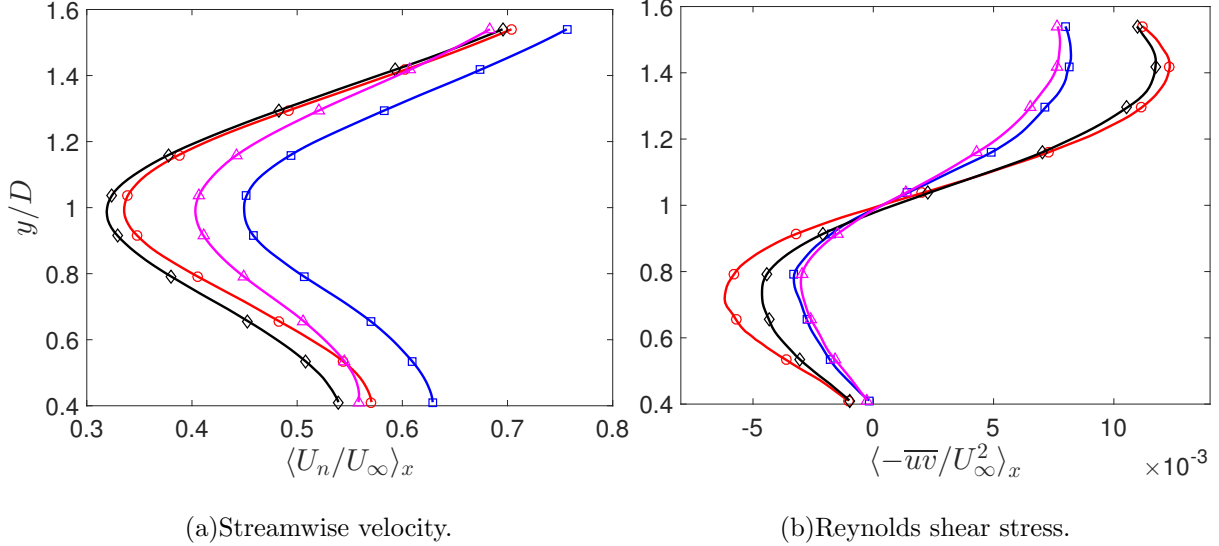


FIG. 7: Streamwise-averaged profiles of streamwise velocity, and Reynolds shear stress for four different cases  $C_{6 \times 3}$  ( $\square$ ),  $C_{3 \times 3}$  ( $\circ$ ),  $C_{3 \times 1.5}$  ( $\diamond$ ), and  $C_{6 \times 1.5}$  ( $\triangle$ ).

237 as it interacts with wakes from the other various turbines thus suppressing the development  
 238 in the streamwise and spanwise direction. Therefore, a reduction in the spanwise turbine-  
 239 to-turbine distance increases the lateral interactions.

240 Figure 7(b) contains the streamwise-averaged Reynolds shear stress  $\langle -\overline{uv}/U_\infty^2 \rangle_x$  for cases  
 241  $C_{6 \times 3}$  through  $C_{6 \times 1.5}$ . Slightly decreased in  $\langle -\overline{uv}/U_\infty^2 \rangle_x$  are attained in case  $C_{6 \times 1.5}$ , where the  
 242 spanwise spacing is reduced. Reducing spanwise spacing shows an important influence when  
 243 the streamwise spacing is  $x/D = 3$ . The streamwise spacing plays a larger role than the  
 244 spanwise spacing, *i.e.* the maximum differences between the Reynolds shear stress profiles  
 245 are detected between cases  $C_{6 \times 3}$  and  $C_{3 \times 3}$ . Interestingly, the largest difference between the  
 246 spatially-averaged Reynolds shear stress is found between cases  $C_{6 \times 3}$  and  $C_{3 \times 3}$ , located at  
 247  $y/D \approx 0.7$  and  $y/D \approx 1.4$ . Furthermore, the four cases have approximately zero Reynolds  
 248 shear stress at the inflection point located at hub height. In addition, case  $C_{3 \times 3}$  displays  
 249 the maximum Reynolds stress and case  $C_{6 \times 1.5}$  presents the minimum stress.

### 250 C. Proper Orthogonal Decomposition.

251 Based on the velocity field, the spatially integrated turbulent kinetic energy is expressed  
 252 by the eigenvalue of each POD mode. The normalized cumulative energy fraction  $\eta_n$  for  
 253 upstream and downstream measurement windows are presented in figure 8(a) and (b), re-

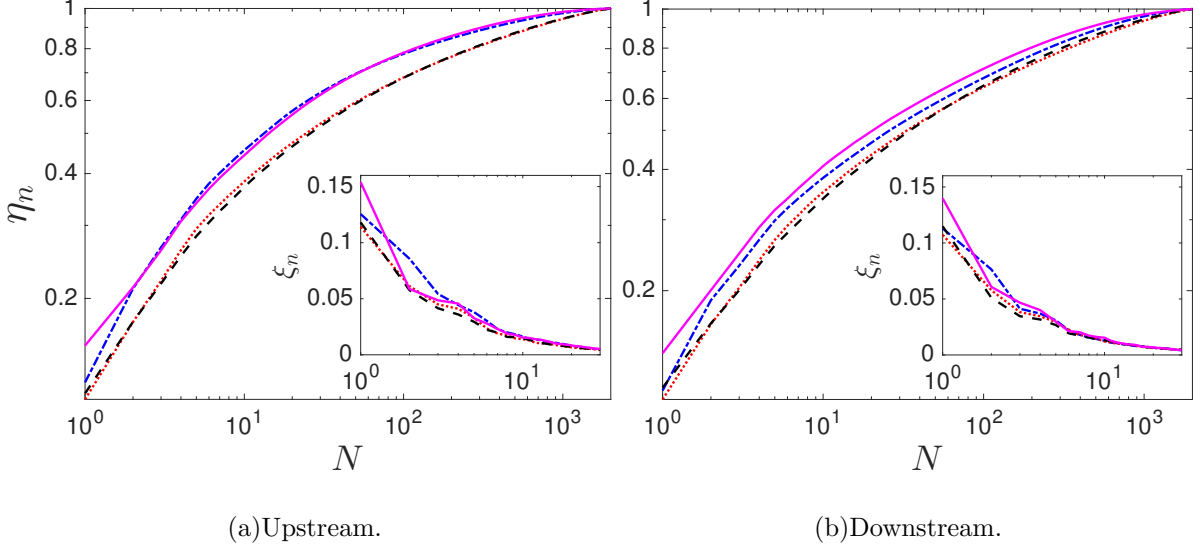


FIG. 8: Energy content of the POD modes for four different cases:  $C_{6 \times 3}$  ( $-\cdot-$ ),  $C_{3 \times 3}$  ( $\cdot\cdot\cdot$ ),  $C_{3 \times 1.5}$  ( $---$ ), and  $C_{6 \times 1.5}$  ( $-$ ).

254 spectively. Inset figures exhibit the normalized energy content per mode,  $\xi_n$ . Upstream of  
 255 the turbine, cases  $C_{6 \times 3}$  and  $C_{6 \times 1.5}$  converge faster than cases  $C_{3 \times 3}$  and  $C_{3 \times 1.5}$ , respectively.  
 256 These results are attributed to the reduction on the streamwise spacing. The convergence  
 257 of case  $C_{3 \times 3}$  is approximately coincident with case  $C_{3 \times 1.5}$ . For the downstream flow, case  
 258  $C_{6 \times 1.5}$  converges faster than the other cases, thereafter it is ordered as  $C_{6 \times 3}$ ,  $C_{3 \times 3}$  and  $C_{3 \times 1.5}$   
 259 in succession. The comparison between the upstream and downstream windows reveals that  
 260 energy accumulates in fewer modes upstream in each case, *e.g.*, case  $C_{6 \times 3}$  requires 14 modes  
 261 to obtain 50% of the total kinetic energy in the upstream window, whereas 26 modes are  
 262 required to obtain the same percentage of energy downstream of the turbine. Cases  $C_{6 \times 1.5}$   
 263 and  $C_{3 \times 1.5}$  show the maximum and minimum variations in  $\lambda_1$ , respectively. This observation  
 264 can be attributed to the structure of the upstream flow of case  $C_{6 \times 1.5}$ , which is rather recov-  
 265 ered, compared to the downstream flow, where the turbulence is high in energy content and  
 266 more complex. However, the upstream and downstream windows of case  $C_{3 \times 1.5}$  are more  
 267 similar in terms of turbulence and organization. From mode 2 through 10, the starkest dif-  
 268 ference between the upstream and downstream is found in case  $C_{6 \times 3}$ . Increasing the spacing  
 269 area per turbine provides room for the flow to become more homogeneous in the upstream  
 270 window and exhibit the most significant momentum deficit in the wake, accounting for the  
 271 differences seen in  $\eta_n$  upstream and downstream.

272 The streamwise component of several POD modes is shown for all cases in figures 9

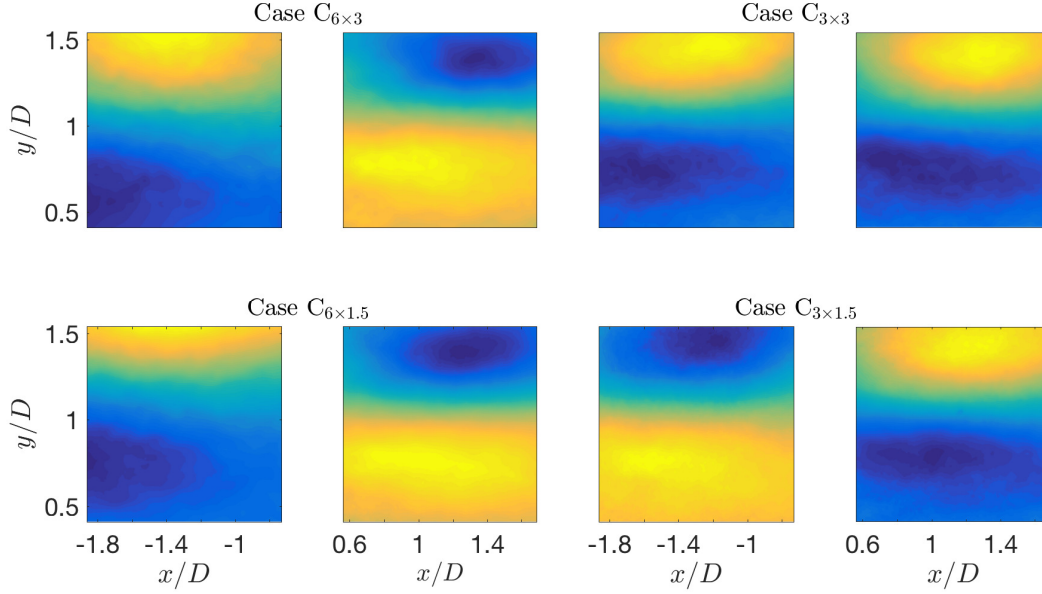


FIG. 9: The first mode upstream and downstream of the each case.

273 through 11. These modes are selected because they provide a range of large and intermedi-  
 274 ate scales, and highlight the discrepancies among the cases. Figure 9 presents the first POD  
 275 mode at the upstream and downstream of the considered cases. The four cases show small  
 276 gradients in the streamwise direction compared to a large gradient in the wall-normal direc-  
 277 tion. Although the four cases show a divergence between the eigenvalues of the first mode,  
 278 the eigenfunctions display very similar structures. For case  $C_{6 \times 3}$  energy of the first POD  
 279 mode shows decreases by 1.25% comparing the upstream eigenvalue to the downstream one,  
 280 see figure 8. Smaller variations of 0.68% and 0.32% are observed in the cases  $C_{3 \times 3}$  and  $C_{3 \times 1.5}$ ,  
 281 respectively. Consequently, the structures of upstream and downstream of these cases are  
 282 approximately equivalent. The similarity in the shape of the structure is observed between  
 283 cases  $C_{6 \times 3}$  and  $C_{6 \times 1.5}$  despite the turbulence kinetic energy difference between them being  
 284 about 3%. The upstream of cases  $C_{6 \times 3}$  and  $C_{6 \times 1.5}$  is representative of the recovering part of  
 285 the flow, in contrast to the downstream that presents the wake region. This difference in the  
 286 physical space has an impact in the low number POD modes that show the discrepancy in  
 287 the coherent structures between the upstream and downstream. In the  $C_{3 \times 3}$  arrangement,  
 288 upstream and downstream both contain similar behaviors, thus pointing to the resemblance  
 289 in the structure. Alike observations can be extracted from case  $C_{3 \times 1.5}$ . Of note, a difference  
 290 in sign of the eigenvectors is present, which is one of the POD properties.

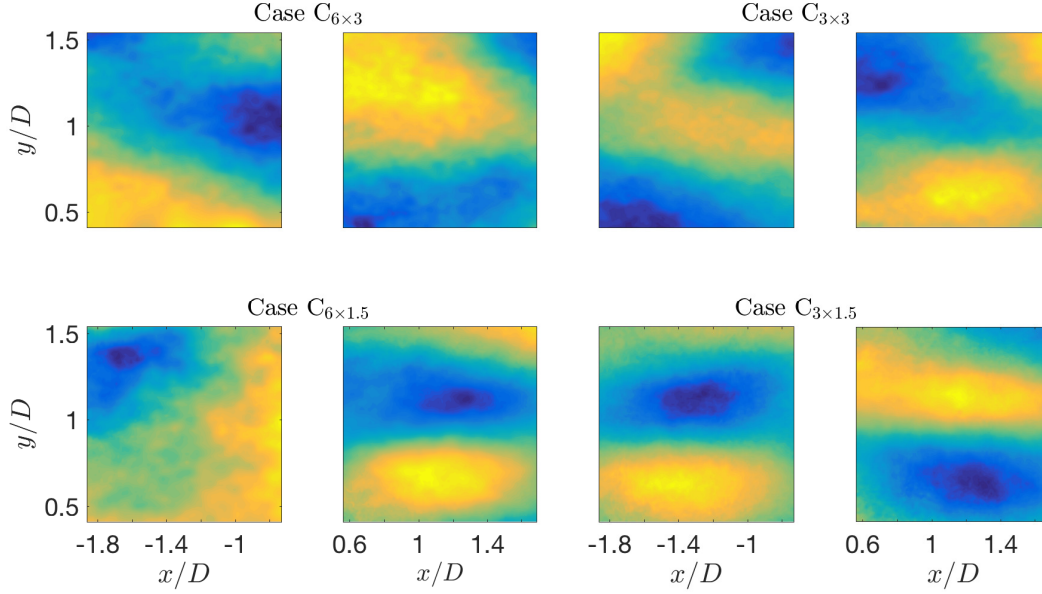


FIG. 10: The fifth mode upstream and downstream of the each case.

291 Figure 10 presents the fifth POD mode of the four cases that show a combination of POD  
 292 and Fourier (homogenous) modes in the streamwise direction. Although the fifth mode of the  
 293 four cases contains  $\approx 74\%$  less energy of than the first mode, large scales are still pronounced.  
 294 Smaller features also appear in the upstream and the downstream windows. The upstream  
 295 window of cases  $C_{6 \times 3}$ ,  $C_{3 \times 3}$ , and  $C_{3 \times 1.5}$  is shifted horizontally in the downstream window.  
 296 The upstream and downstream widows of case  $C_{3 \times 1.5}$  look like the first mode, but at a  
 297 reduced scale. The same trend is observed in the downstream window of the case  $C_{6 \times 1.5}$ .

298 Figure 11 presents the twentieth POD mode, where small structures become noticeable  
 299 in both upstream and downstream windows. The upstream measurement window of cases  
 300  $C_{6 \times 3}$  and  $C_{6 \times 1.5}$  shows large scale structures compared with the other two cases. Although,  
 301 after mode 10, there is no significant difference in the energy content from case to case, the  
 302 structure of the modes shows a significant discrepancy between the cases confirming that  
 303 the intermediate modes are associated with the inflow characterizations.

#### 304 D. Reconstruction of Averaged Profile.

305 Combining the POD modes with the corresponding time coefficient gives these modes the  
 306 physical interpretation and shows the contribution of these modes in the flow perturbation.

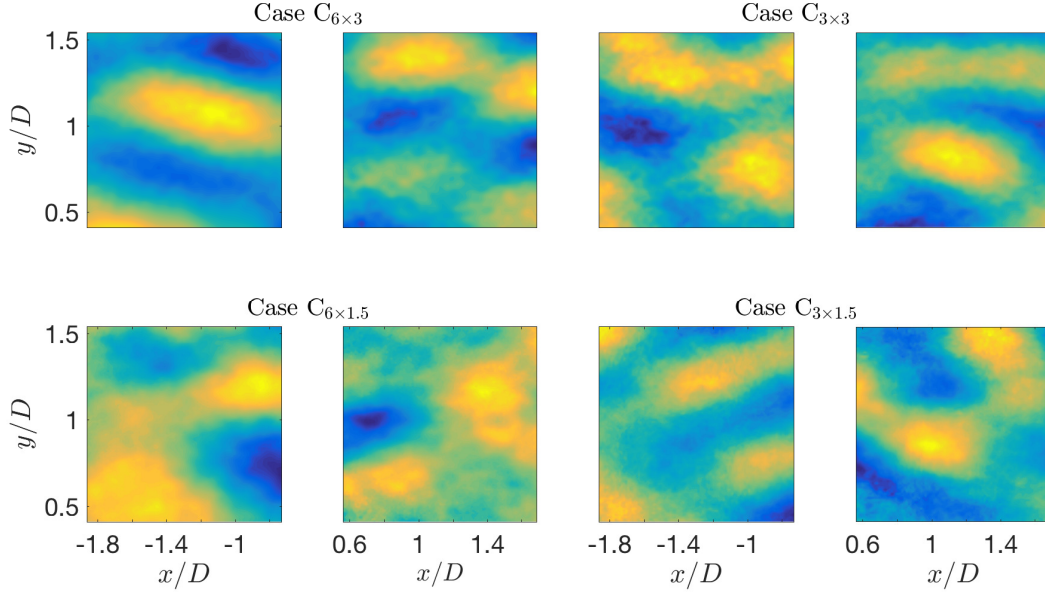


FIG. 11: The twentieth mode upstream and downstream of the each case.

307 A reduced degree of the turbulence kinetic energy is considered using only a few modes  
 308 to reconstruct the streamwise-averaged profiles of Reynolds shear stress. Reconstructions  
 309 are made using either the first mode, the first 5, 10, 25, or 50 modes to represent the  
 310 stress as shown in figure 12. Inset figures present the Reynolds shear stress construction  
 311 using the modes 5-10, 5-25, and 5-50, respectively, excluding the first four modes isolates  
 312 contributions from intermediate modes. The black lines are the streamwise average of full  
 313 data from figure 7(b). Using an equal number of modes, case  $C_{6 \times 1.5}$  rebuilds the profiles  
 314 of the Reynolds shear stress faster than the other cases. Case  $C_{6 \times 3}$  also shows the fast  
 315 reconstruction and the dissimilarity with case  $C_{6 \times 1.5}$  is mainly in the profile of first mode  
 316 (red line) and the first five modes (blue line). Cases  $C_{3 \times 3}$  and  $C_{3 \times 1.5}$  show approximately  
 317 the same trends in reconstruction profiles. Below hub height, the four cases show the same  
 318 trend of the first mode profiles, where the contribution in the reconstruction profiles is zero.  
 319 The first five modes display exactly the form of the full data profile of individual case. The  
 320 maximum difference between the successive reconstruction profiles occurs between the first  
 321 mode and the first five modes. The cases  $C_{6 \times 3}$ ,  $C_{3 \times 3}$  and  $C_{3 \times 1.5}$  show moderate variation  
 322 between the profiles of the reconstructed stress resulting from first five and first ten modes  
 323 (red and green lines, respectively). After mode 10 contributions by each additional mode  
 324 are quite small, shown by pink and gray lines.

325 The maximum difference between the full data and the reconstructed profiles is located  
 326 at  $y/D \approx 0.75$  and  $y/D \approx 1.4$ , where the extrema in  $\langle -\overline{uv} \rangle_x$  are located. Generally, faster  
 327 reconstruction implies that the flow possesses coherent structures with a greater portion of  
 328 the total kinetic energy. Consequently, the flow characterized with greater coherence in the  
 329 cases  $C_{6 \times 3}$  and  $C_{6 \times 1.5}$ . In cases  $C_{3 \times 3}$  and  $C_{3 \times 1.5}$ , less energetic features are observed due to the  
 330 reduced spacing effect that leads to a reduction of the mean velocities within the canopy and  
 331 an increase in lateral wake interactions. These interactions, which become larger as a result  
 332 of the accumulated wakes, expand downstream of the rotor. Thus, the streamwise spacing  
 333 allows for the flow to recover and therefore produce larger, more coherent structures within  
 334 the domain, which in comparison eclipses variations produced by the spanwise spacing. Also,  
 335 the large spacing offers a larger frontal area to the wind coming from above the lateral sides.

336 To quantify the contribution of the moderate-scaled structures, Reynolds shear stress is  
 337 reconstructed using the intermediate modes. As can be shown in the insets of figure 12,  
 338 the full data profile (black line) is compared with profiles reconstructed from modes 5-10  
 339 (red line), 5-25 (blue line), and 5-50 (green lines). The intermediate modes in each case  
 340 approximately take the form of the full data profiles below the hub height, although the  
 341 magnitudes of the reconstructions are smaller than those of the full data statistics. Recon-  
 342 struction Reynolds shear stress in cases  $C_{6 \times 3}$  and  $C_{3 \times 1.5}$  show minute variations between  
 343 the successive reconstruction profiles and are essentially vertical lines above the hub height.  
 344 This trend is opposite to the trend that is shown in the first mode profile. Cases  $C_{3 \times 3}$  and  
 345  $C_{3 \times 1.5}$  show a difference between the successive profiles above the hub height. The maximum  
 346 difference is observed between the reconstructed profiles from modes 5-10 and from 5-25 due  
 347 to the turbulence kinetic energy contained within these modes.

### 348 E. Anisotropy Stress Tensor

349 To examine the dynamics and energy transfer in the wind turbine arrays with different  
 350 streamwise and spanwise spacings, a description of the anisotropy in the upstream and  
 351 downstream of the wind turbines is presented in figure 13. A visualization of the turbulence  
 352 state is obtained via the color map representing the barycentric map as described in section  
 353 II B, where it efficiently distinguishes among the cases in terms of wake propagation and wake  
 354 interaction. The variation in the spacings changes the background turbulence structure.

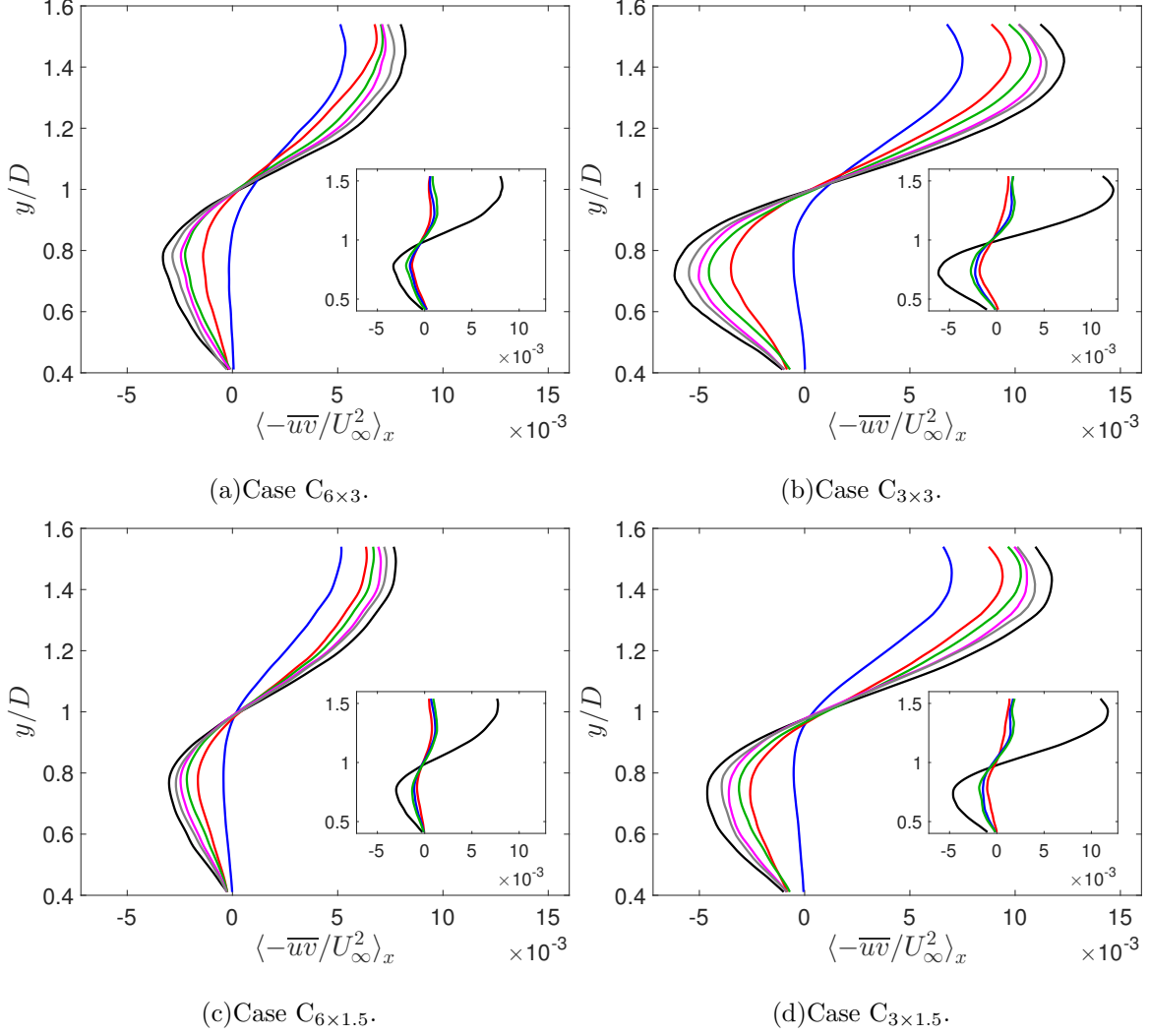


FIG. 12: Reconstruction Reynolds shear stress using: first mode (—), first 5 modes (—), first 10 modes (—), first 25 modes (—) and first 50 modes (—). Full data statistics (—). The insets show the reconstruction using modes 5-10 (—), 5-25 (—), and 5-50 (—).

355 The upstream of cases  $C_{6 \times 3}$  and  $C_{6 \times 1.5}$  shows the turbulence state close to the isotropy limit  
 356 especially in hub height region as a result of the wake recovery occurring under a relatively  
 357 long spacing distance. Below the bottom tip, these cases show pancake-like turbulence due to  
 358 the surface effect that appear deeming the perturbation of the turbines virtually negligible.  
 359 Near top tip, the flow shows a turbulence of axisymmetric state (between the pancake-like  
 360 and cigar-like turbulence). With this representation, the spacing variation leads to a changed  
 361 state of the turbulence and between the developed and developing flow conditions can be  
 362 discernible. The upstream of case  $C_{3 \times 3}$  shows a pancake-like turbulence state. However,  
 363 the hub height and bottom tip regions shows an isotropic and axisymmetric turbulence,

364 respectively. The upstream of case  $C_{3 \times 1.5}$  exhibits axisymmetric and cigar-like turbulence  
365 in the most of the upstream domain, although the hub height region remains described by  
366 isotropic turbulence.

367 Past the turbine, the four cases exhibit the turbulence of isotropic state in the hub height  
368 region. The top tip region of the four cases shows axisymmetric turbulence although case  
369  $C_{3 \times 3}$  tends to be a cigar-like turbulence. Below the hub height, the turbulence is pancake-  
370 like and the difference amongst the cases is the covered area, where it is maximum at  $C_{6 \times 3}$   
371 and minimum at  $C_{3 \times 3}$ . The longest extension is found in case  $C_{6 \times 3}$  and the lowest in case  
372  $C_{3 \times 3}$  with. Comparing to  $C_{6 \times 3}$ , the change seen in the turbulence states is starker in  $C_{3 \times 3}$   
373 than in  $C_{6 \times 1.5}$ , confirming that the impact of reducing streamwise spacing is greater than  
374 changing the spanwise spacing. However, the impact of the spanwise spacing is noticeable  
375 when  $S_x$  equals  $3D$ .

376 The ability to identify the turbulence structure allows for identification of its influence  
377 on subsequent turbines in terms of fatigue loads (Frandsen and Thøgersen 1999). Further,  
378 regions of the flow that are characterized by highly anisotropic turbulence are those in which  
379 one is likely to find large-scale, coherent turbulence structures. These structures impart  
380 the greatest axial and bending loads onto subsequent turbine rotors leading to accelerated  
381 fatigue and increased operational and maintenance costs for wind farms. In addition, regions  
382 of high anisotropy correlate with gradients in the mean flow and turbulence (Hamilton and  
383 Cal 2015). These quantities are of particular interest in wind farm modeling and design.  
384 Accordingly, the accurate representation of gradients in wind farm design modeling is a  
385 necessary check to accurately representing production of and flux by turbulence kinetic  
386 energy, wake interaction, and structural loading on constituent turbines. Finally, the stress  
387 tensor invariants, by definition, do not depend on reflection or rotation of the coordinate  
388 system meaning that they are unbiased descriptive for the turbulent flow (Pope 2000).

## 389 V. POWER MEASUREMENTS.

390 Figure 14 demonstrates the power produced by each turbine,  $\mathcal{F}_x$ , obtained with the torque  
391 sensing system, versus the angular velocity,  $\omega$ . The power measurements are normalized by  
392 the maximum theoretical power  $\frac{1}{2}\rho A_c U_\infty^3$ , where  $\rho$  is the air density,  $A_c$  is swept area of  
393 the turbine rotor  $\pi D^2/4$ . The angular velocity is normalized by the  $2U_\infty/D$ . It is apparent

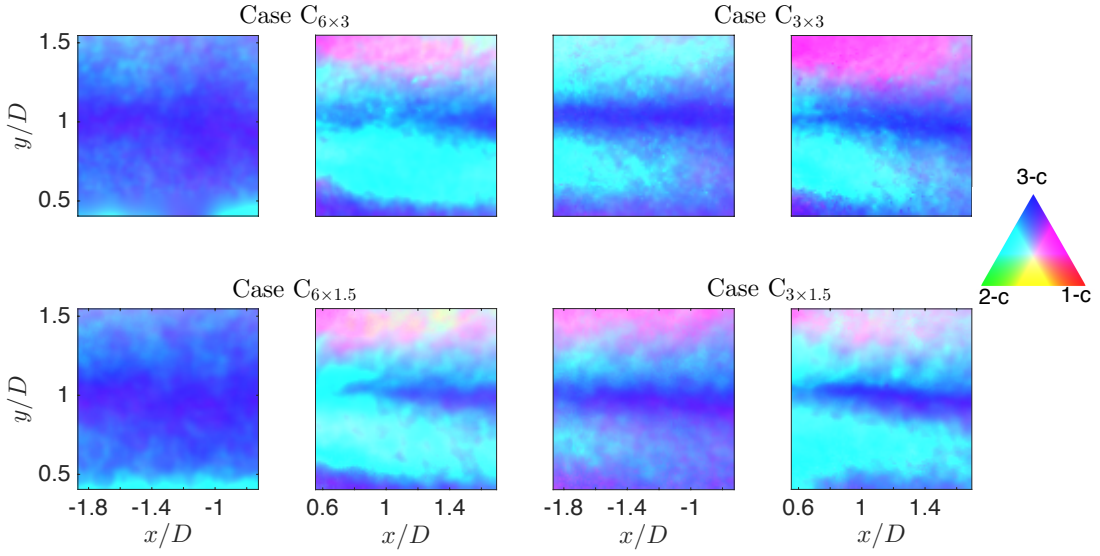


FIG. 13: Barycentric map map for the upstream and downstream of the considered cases. The small triangle is a color map key for ease of interpretation.

394 from the figure that the maximum power is extracted at the normalized angular velocity of  
 395  $15.8 \pm 1$ . The maximum normalized power of 0.062 is harvested at the largest spacing, *i.e.*,  
 396 case  $C_{6 \times 3}$ . Fixing the spanwise spacing and decreasing the streamwise spacing reduces the  
 397 normalized power produced by 33% for  $S_x = 6D$  (from case  $C_{6 \times 3}$  to case  $C_{3 \times 3}$ ) and by 22  
 398 % for  $S_x = 3D$  (from case  $C_{3 \times 1.5}$  to case  $C_{6 \times 1.5}$ ). The complementary change in spacing  
 399 holds the streamwise spacing constant while decreasing the spanwise spacing. In that case  
 400 the normalized power produced is reduced by 20% for  $S_z = 3D$  (from case  $C_{6 \times 3}$  to case  
 401  $C_{6 \times 1.5}$ ) and by 6% for  $S_z = 1.5D$  (from case  $C_{3 \times 3}$  to case  $C_{3 \times 1.5}$ ). Nilsson et al. (2015) has  
 402 complementary results to the ones present, where an increase in power produced is attained  
 403 in the largest spacing and conversely, decreased in the limited spacing case. Furthermore,  
 404 increasing the spanwise distance has a less notable effect in comparison to the streamwise  
 405 spacing.

406 The trend of the power curves follows the one observed in the averaged profiles of the  
 407 streamwise velocity, see figure 7 (a). Further, they verify the relationship between the power  
 408 of the turbine with the deficit velocity. The maximum power and velocity are found in the  
 409 case  $C_{6 \times 3}$  and the minimum quantities are noticed in  $C_{3 \times 1.5}$ . The smallest variations in the  
 410 power measurement and main velocity are observed between cases  $C_{3 \times 3}$  and  $C_{3 \times 1.5}$ , whereas  
 411 the largest difference is observed between cases  $C_{6 \times 3}$  and  $C_{3 \times 3}$ . Increased longitudinal  
 412 spacing produces larger energy content in the first few modes as to provide the imprint

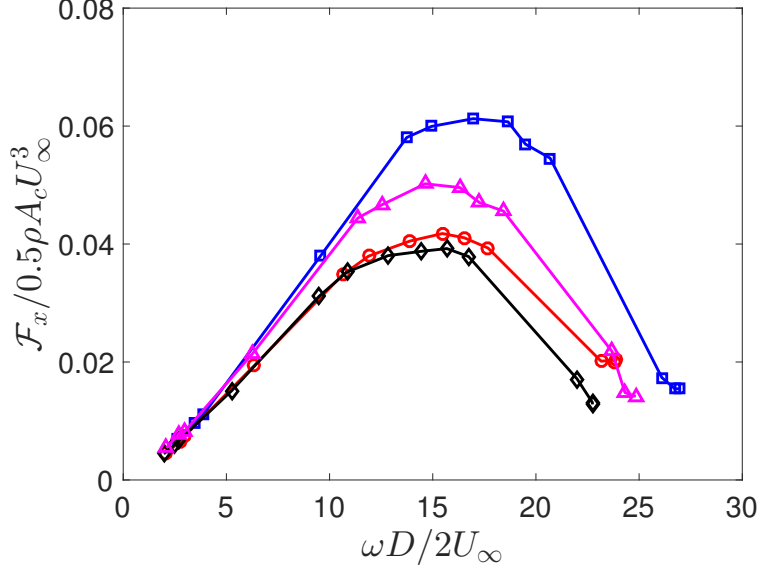


FIG. 14: Extracted power of the wind turbine at different angular velocities for four different cases  $C_{6 \times 3}$  (□),  $C_{3 \times 3}$  (○),  $C_{3 \times 1.5}$  (◇), and  $C_{6 \times 1.5}$  (△).

413 of the flow; thus, this is reflected in an increase in power as directly measured via a torque  
 414 sensing device.

## 415 VI. CONCLUSIONS

416 Insight into the behavior of the flow in a wind turbine array is useful in determining how  
 417 to highlight the overall power extraction with the variation in spacing between the turbines.  
 418 The work above quantifies effects of tightly spaced wind turbine configurations on the flow  
 419 behavior. The findings of this study have a number of important implications, especially  
 420 regarding the cost of a wind farm or when large areas are not available. Stereographic  
 421 PIV data are used to assess characteristic quantities of the flow field in a wind turbine  
 422 array with varied streamwise and spanwise spacing. Four cases of different streamwise and  
 423 spanwise spacings are examined; the streamwise spacing being  $6D$  and  $3D$ , and spanwise  
 424 spacing being  $3D$  and  $1.5D$ . The flow fields are analyzed and compared statistically and by  
 425 snapshot proper orthogonal decomposition.

426 The streamwise mean velocity, and Reynolds shear stress are quantified upstream and  
 427 downstream of the wind turbine in the considered cases. In the inflow measurement window,  
 428 higher velocities are observed in cases  $C_{6 \times 3}$  and  $C_{6 \times 1.5}$  comparing to the other two cases

429 whose inflows are unrecovered wakes from preceding rows. In contrast, case  $C_{3 \times 3}$  and  $C_{3 \times 1.5}$   
 430 show higher Reynolds shear stress. The notable differences between the cases are found  
 431 above the top tip and below the bottom tip downstream the turbines, whereas the core  
 432 of the wakes shows fewer discrepancies. The streamwise and spanwise spacings have a  
 433 concerted effect on the flow, where the degree of the impact of one change highly depends  
 434 on the other. This relationship is shown in all statistical quantities discussed here, such as  
 435 reducing of the streamwise spacing by 50% leads to increases in the averaged Reynolds shear  
 436 stress by 16% when  $S_z = 3D$ . According to current statistical quantities, one can infer that  
 437 the higher influence of streamwise spacing is shown when the spanwise spacing is  $S_z = 3D$ ,  
 438 and the significant effect of the spanwise spacing is observed when the streamwise spacing is  
 439  $S_x = 3D$ . To make comparisons independent of the effects streamwise spacing, streamwise  
 440 average profiles of the statistical quantities are computed. Averaged profiles of the velocity  
 441 follow the order of higher velocity seen in the contour plots in case  $C_{6 \times 3}$  and lowest velocity  
 442 in case  $C_{3 \times 1.5}$ . The maximum and minimum difference are observed between cases  $C_{6 \times 3}$  with  
 443 case  $C_{3 \times 1.5}$  and  $C_{3 \times 3}$  with case  $C_{3 \times 1.5}$ . The result also reveals that the streamwise spacing  
 444 is more impactful than the spanwise spacing. Spatially-averaged profile of Reynolds shear  
 445 stress shows the maximum and minimum values occur in cases  $C_{3 \times 3}$  and  $C_{6 \times 1.5}$ , respectively.

446 Based on the POD analysis, the upstream measurement plane of the four cases converges  
 447 faster than the downstream window. Case  $C_{6 \times 3}$  and  $C_{6 \times 1.5}$  show the rapid convergence in  
 448 cumulative energy content upstream of the turbine, but  $C_{6 \times 3}$  remains behind case  $C_{6 \times 1.5}$  in  
 449 the wake. The first mode of the case  $C_{6 \times 1.5}$  carries the maximum turbulent kinetic energy  
 450 content compared to the first mode of the other cases. No significant difference in energy  
 451 content is observed after mode 10 between the four cases. The streamwise-averaged profiles  
 452 of the Reynolds shear stress are reconstructed by back-projecting coefficients onto the set of  
 453 eigenfunctions. Low modes are used individually to demonstrate their contributions to the  
 454 overall flow. Cases  $C_{6 \times 1.5}$  and  $C_{6 \times 3}$  converge to the total spatially-averaged profile faster  
 455 than other two cases and the discrepancy in reconstruction is mainly observed in profiles  
 456 using only the first five modes. The same trend in reconstruction is observed in cases  $C_{3 \times 3}$   
 457 and  $C_{3 \times 1.5}$ . Reconstructed profiles display the effects of the spacing, where the array of large  
 458 streamwise spacing reconstruct faster than the other cases due to the coherent structures  
 459 embedded within the flow.

460 Based on the anisotropy stress tensor and color map visualization, the spacing modifies

461 the turbulence structure and the longest spacing attenuates the perturbation of the turbu-  
462 lence, inducing the flow towards a more isotropic state. The hub height region shows an  
463 isotropic turbulence state regardless the spacing. The differences of the color map visualiza-  
464 tion between the downstream locations of the four cases show some structural dependency  
465 on the spacing between turbine rotors.

466 Power production by the turbines is measured directly using torque sensing system. The  
467 power curves follow the same trend as the velocity profiles. The maximum power extracted  
468 at the normalized angular velocity of  $15.8 \pm 1$  and it is harvested in case  $C_{6 \times 3}$ . The small  
469 difference in harvested power is observed between cases  $C_{3 \times 3}$  and  $C_{3 \times 1.5}$ . The current work  
470 demonstrates that wake statistics and power produced by a wind turbine depend more on  
471 streamwise spacing than spanwise spacing. However, results above pertain only to a fixed  
472 inflow direction. In the case where the bulk flow orientation changes, spacing in both the  
473 streamwise and spanwise directions will be important to the optimal power production in  
474 a wind turbine array. Continued efforts are required to understand the impact of stream-  
475 wise and spanwise spacing in infinite array flow with Coriolis forcing and under different  
476 stratification conditions.

## 477 Acknowledgments

478 Naseem Ali acknowledges support from the Higher Committee of Education Development  
479 in Iraq (HCED). The authors are grateful to NSF-ECCS-1032647 for funding this research.

---

480 B. Viggiano, M. S. Gion, N. Ali, M. Tutkun, and R. B. Cal, *Journal of Renewable and Sustainable*  
481 *Energy* **8**, 053310 (2016).

482 N. Ali, A. S. Aseyev, and R. B. Cal, *Journal of Renewable and Sustainable Energy* **8**, 013304  
483 (2016a).

484 R. J. Barthelmie, S. T. Frandsen, M. N. Nielsen, S. C. Pryor, P.-E. Rethore, and H. E. Jørgensen,  
485 *Wind Energy* **10**, 517 (2007).

486 L. P. Chamorro and F. Porté-Agel, *Boundary-layer meteorology* **132**, 129 (2009).

487 L. P. Chamorro and F. Porté-Agel, *Energies* **4**, 1916 (2011).

488 R. J. Barthelmie, S. C. Pryor, S. T. Frandsen, K. S. Hansen, J. G. Schepers, K. Rados, W. Schlez,  
489 A. Neubert, L. E. Jensen, and S. Neckelmann, *Journal of Atmospheric and Oceanic Technology*  
490 **27**, 1302 (2010).

491 R. J. Barthelmie and L. E. Jensen, *Wind Energy* **13**, 573 (2010).

492 K. S. Hansen, R. J. Barthelmie, L. E. Jensen, and A. Sommer, *Wind Energy* **15**, 183 (2012).

493 F. González-Longatt, P. Wall, and V. Terzija, *Renewable Energy* **39**, 329 (2012).

494 J. Meyers and C. Meneveau, *Wind Energy* **15**, 305 (2012).

495 R. J. Stevens, *Wind Energy* p. 10.1002/we.1857 (2015).

496 D. Romanic, D. Parvu, M. Refan, and H. Hangan, *Renewable Energy* **115**, 97 (2018).

497 K. Nilsson, S. Ivanell, K. S. Hansen, R. Mikkelsen, J. N. Sørensen, S.-P. Breton, and D. Henningson,  
498 *Wind Energy* **18**, 449 (2015).

499 J. Meyers and C. Meneveau, *AIAA* **827**, 2010 (2010).

500 X. Yang, S. Kang, and F. Sotiropoulos, *Physics of Fluids (1994-present)* **24**, 115107 (2012).

501 Y.-T. Wu and F. Porté-Agel, *Boundary-Layer Meteorology* **146**, 181 (2013).

502 C. L. Archer, S. Mirzaeisefat, and S. Lee, *Geophysical Research Letters* **40**, 4963 (2013).

503 R. J. Stevens, D. F. Gayme, and C. Meneveau, *Wind Energy* **19**, 359 (2016).

504 J. L. Lumley, *Atmospheric Turbulence and Radio Wave Propagation* pp. 166–178 (1967).

505 L. Sirovich, *Quarterly of Applied Mathematics* **45**, 561 (1987).

506 M. N. Glauser and W. K. George, in *Advances in Turbulence* (Springer, 1987), pp. 357–366.

507 P. Moin and R. D. Moser, *Journal of Fluid Mechanics* **200**, 471 (1989).

508 S. Shah and E. Bou-Zeid, *Boundary-Layer Meteorology* **153**, 355 (2014).

509 M. Tutkun, P. B. Johansson, and W. K. George, *AIAA* **46**, 1118 (2008).

510 S. J. Andersen, J. N. Sørensen, and R. Mikkelsen, *Journal of Turbulence* **14**, 1 (2013).

511 D. Bastine, B. Witha, M. Wächter, and J. Peinke, *Journal of Physics: Conference Series* **524**,  
512 012153 (2014).

513 C. VerHulst and C. Meneveau, *Physics of Fluids* **26**, 025113 (2014).

514 N. Hamilton, M. Tutkun, and R. B. Cal, *Wind Energy* **18**, 297 (2015a).

515 N. Ali, H. F. Kadum, and R. B. Cal, *Journal of Renewable and Sustainable Energy* **8**, 063306  
516 (2016b).

517 N. Ali, G. Cortina, N. Hamilton, M. Calaf, and R. B. Cal, *Journal of Fluid Mechanics* **828**, 175  
518 (2017a).

519 J. Rotta, *Z. Physik* **131** (1951).

520 S. B. Pope, *Turbulent flows* (Cambridge University Press, 2000).

521 J. L. Lumley and G. R. Newman, *Journal of Fluid Mechanics*. **82**, 161 (1977).

522 S. Banerjee, R. Krahl, F. Durst, and C. Zenger, *Journal of Turbulence* **8**, N32 (2007).

523 M. Emory and G. Iaccarino, Annual Brief, Center for Turbulence Research (2014).

524 R. A. Antonia, J. Kim, and L. Browne, *Journal of Fluid Mechanics*. **233**, 369 (1991).

525 P. Krogstad and L. E. Torbergsen, *Flow, turbulence and combustion*. **64**, 161 (2000).

526 C. Klipp, in *SPIE Defense, Security, and Sensing*. (International Society for Optics and Photonics.,  
527 2010), pp. 768505–768505.

528 C. Klipp, in *SPIE Defense, Security, and Sensing*. (International Society for Optics and Photonics.,  
529 2012), p. 83800G.

530 R. Gómez-Elvira, A. Crespo, E. Migoya, F. Manuel, and J. Hernández, *Journal of Wind Engineering*  
531 *and Industrial Aerodynamics*. **93**, 797 (2005).

532 N. Hamilton and R. B. Cal, *Physics of Fluids*. **27**, 015102 (2015).

533 N. Ali, A. S. Aseyev, M. S. Melius, M. Tutkun, and R. B. Cal, in *Whither Turbulence and Big*  
534 *Data in the 21st Century?* (Springer, 2017b), pp. 273–292.

535 N. Ali, N. Hamilton, G. Cortina, M. Calaf, and R. B. Cal, *Journal of Renewable and Sustainable*  
536 *Energy* **9** (2017c).

537 L. P. Chamorro, R. Arndt, and F. Sotiropoulos, *Wind Energy* **15**, 733 (2012).

538 R. B. Cal, J. Lebrón, L. Castillo, H. S. Kang, and C. Meneveau, *Journal of Renewable and*  
539 *Sustainable Energy* **2**, 013106 (2010).

540 H. S. Kang and C. Meneveau, *Measurement Science and Technology* **21**, 105206 (2010).

541 N. Hamilton, M. Melius, and R. B. Cal, *Wind Energy* **18**, 277 (2015b).

542 W. K. George, Chalmers University of Technology (2013).

543 S. Frandsen and M. L. Thøgersen, *Wind Engineering* pp. 327–339 (1999).